Atmospheric
Chemistry
and Physics

Inverse modeling of Texas NO_x emissions using space-based and ground-based NO_2 observations

W. Tang[1], **D. S. Cohan**[1], **L. N. Lamsal**[2,3], **X. Xiao**[1], **and W. Zhou**[1]

[1]Department of Civil and Environmental Engineering, Rice University, 6100 Main Street MS 519, Houston, TX 77005, USA
[2]NASA Goddard Space Flight Center, Greenbelt, MD, USA
[3]Goddard Earth Sciences Technology & Research, Universities Space Research Association, Columbia, MD, USA

Correspondence to: W. Tang (wei.tang@rice.edu)

Abstract. Inverse modeling of nitrogen oxide (NO_x) emissions using satellite-based NO_2 observations has become more prevalent in recent years, but has rarely been applied to regulatory modeling at regional scales. In this study, OMI satellite observations of NO_2 column densities are used to conduct inverse modeling of NO_x emission inventories for two Texas State Implementation Plan (SIP) modeling episodes. Addition of lightning, aircraft, and soil NO_x emissions to the regulatory inventory narrowed but did not close the gap between modeled and satellite-observed NO_2 over rural regions. Satellite-based top-down emission inventories are created with the regional Comprehensive Air Quality Model with extensions (CAMx) using two techniques: the direct scaling method and discrete Kalman filter (DKF) with decoupled direct method (DDM) sensitivity analysis. The simulations with satellite-inverted inventories are compared to the modeling results using the a priori inventory as well as an inventory created by a ground-level NO_2-based DKF inversion. The DKF inversions yield conflicting results: the satellite-based inversion scales up the a priori NO_x emissions in most regions by factors of 1.02 to 1.84, leading to 3–55 % increase in modeled NO_2 column densities and 1–7 ppb increase in ground 8 h ozone concentrations, while the ground-based inversion indicates the a priori NO_x emissions should be scaled by factors of 0.34 to 0.57 in each region. However, none of the inversions improve the model performance in simulating aircraft-observed NO_2 or ground-level ozone (O_3) concentrations.

1 Introduction

Nitrogen oxides ($NO_x = NO + NO_2$) in the troposphere are primary air pollutants, emitted from both anthropogenic sources like fossil-fuel combustion and biomass burning, and natural sources such as soil microbial processes and lightning. NO_x also acts as a precursor of a secondary air pollutant, tropospheric O_3, when it reacts with the oxidation products of volatile organic compounds (VOCs) in the presence of sunlight. Oxidation with hydroxyl (OH) radical is the dominant sink of NO_x, leading to atmospheric nitric acid (HNO_3) formation. The atmospheric lifetime of tropospheric NO_x varies from a few hours in summer to a couple of days in winter (Seinfeld and Pandis, 2006).

NO_x emission inventories used in air quality modeling are typically developed by a bottom-up approach based on estimated activity rates and emission factors for each category. Due to inaccuracies in determining these rates and factors, the uncertainty in NO_x emission inventories has been suggested to be as high as a factor of two and classified as one of the top uncertainties in ozone simulations and sensitivity analysis (Hanna et al., 2001; Xiao et al., 2010).

Inverse modeling techniques can be used with atmospheric models to estimate model variables that may not be directly measurable (Gilliland and Abbitt, 2001). Inverse modeling generates an optimized "top-down" NO_x emission inventory for air quality models by minimizing the difference between observed and modeled NO_2 concentrations, providing an opportunity to identify possible biases in the bottom-up NO_x emission inventory (Napelenok et al., 2008). However, as uncertainties may also be associated with the measurement

data and the inverse methods themselves, inverse modeling has its own limitations. Hence, it is valuable to compare both bottom-up and top-down NO$_x$ emission inventories in order to improve the understanding of NO$_x$ emissions.

Several inverse modeling studies have used surface NO$_2$ measurements (Mendoza-Dominguez and Russell, 2000; Quélo et al., 2005; Pison et al., 2007) or aircraft NO$_2$ measurements (Brioude et al., 2011) to constrain NO$_x$ emissions. Compared to ground and aircraft measurements, satellite-based observations generate greater spatial coverage of NO$_2$. Studies on combining satellite NO$_2$ measurements with inverse modeling techniques to create the top-down NO$_x$ emission inventories also have been conducted recently in both global scale (Martin et al., 2003; Müller and Stavrakou, 2005; Jaeglé et al., 2005; Lin et al., 2010) and regional scale modeling (Konovalov et al., 2006, 2008; Deguillaume et al., 2007; Napelenok et al., 2008; Kurokawa et al., 2009; Zhao and Wang, 2009; Chai et al., 2009).

Discrete Kalman filter (DKF) (Prinn, 2000) is an inverse modeling method that solves the inverse problem iteratively, and can be applied to the cases with linear or weakly nonlinear relationships between emissions and pollutants. It has been used in several studies to constrain emissions of carbon monoxide (Mulholland and Seinfeld, 1995), chlorofluorocarbons (Haas-Laursen et al., 1996), isoprene (Chang et al., 1996) and ammonia (Gilliland et al., 2003). Most recently, Napelenok et al. (2008) applied the DKF method to the regional Community Multiscale Air Quality (CMAQ) model, generating a top-down NO$_x$ emission inventory for the southeastern United States using Scanning Imaging Absorption Spectrometer for Atmospheric Chartography (SCIAMCHY) (Bovenmann et al., 1999) satellite NO$_2$ data.

Despite the growing number of scientific studies conducting satellite-based inversions of NO$_x$ emissions, the applicability of these methods to state-level regulatory attainment modeling has not been widely explored. In this work, the DKF method introduced by Napelenok et al. (2008) is applied with finer-resolution satellite NO$_2$ data now available from the Ozone Monitoring Instrument (OMI) as well as ground-level NO$_2$ observations, to constrain NO$_x$ emissions for actual regulatory modeling episodes in Texas. Lightning and aircraft NO$_x$ emissions are added to the base case NO$_x$ emission inventory to address the bias noted by Napelenok et al. (2008) of regional models underestimating upper tropospheric NO$_x$. The DKF inverted a posteriori emissions are compared to the base case emissions, the a priori emissions and a posteriori emissions derived by the inversion method of Martin et al. (2003).

2 Methodology

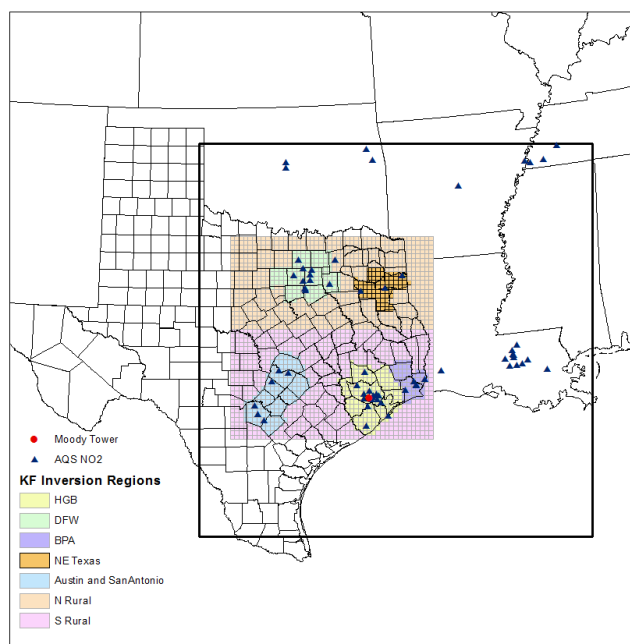### 2.1 Model inputs and configurations

Base case model inputs were taken from episodes developed by the Texas Commission on Environmental Quality (TCEQ) for Texas ozone attainment planning. CAMx version 5.3 (ENVIRON, 2010) was used in this study to simulate two modeling episodes in 2006 with high ozone concentrations in the Dallas–Fort Worth (DFW) region, from 31 May to 1 July, hereafter referred to as the June episode, and in the Houston–Galveston–Brazoria (HGB) region, from 13 August to 15 September (Fig. 1), hereafter referred to as August–September episode. The NCAR/Penn State (National Center for Atmospheric Research/Pennsylvania State University) Mesoscale Model, version 5, release 3.7.3 (MM5v.3.7.3) (Grell et al., 1994), conducted with the ACM2 scheme for the June episode and the Eta scheme for the August–September episode, was used to generate the meteorological fields with 43 vertical layers. The preprocessor MM5CAMx was used to convert MM5 outputs into CAMx-ready meteorology inputs. The modeled meteorological parameters: temperature, wind speed, wind direction, and planetary boundary layer (PBL) height in both episodes are evaluated as shown in the Supplementary Sect. 1. The vertical configuration of CAMx modeling consists of 17 vertical layers for the August–September modeling episode, whereas 28 vertical layers were used for the June modeling episode. Modeling was conducted with the Carbon Bond version 2005 (CB-05) chemical mechanism, PPM advection scheme, and K-theory vertical diffusion scheme (TCEQ, 2010, 2011). Boundary conditions for the 36 km eastern US domain were generated by the Model for Ozone and Related Chemical Tracers (MOZART) global model (ENVIRON, 2008).

2.2 Emission inventory

Base case emission inventories were provided by TCEQ (Table 1). The point source emissions were from the State of Texas Air Reporting System (STARS) database, which collects emission information from approximately 2000 point sources annually, and the EPA's acid rain database (ARD), which contains emissions from electric generating units (EGUs). The on-road mobile emission inventory was generated by Motor Vehicle Emission Simulator 2010a (MOVES2010a), and the non-road mobile inventory was developed by National Mobile Inventory Model (NMIM) and the Texas NONROAD (TexN) mobile source model. The area source inventory was projected by the EPA Economic Growth Analysis System (EGAS) model based on 2005 emissions from the Texas Air Emissions Repository (Tex-AER) database. The Emission Processing System, version 3 (EPS3) (ENVIRON, 2007), was used for processing the point, mobile, and area emissions to the model-ready format (TCEQ, 2010, 2011). Biogenic emissions were generated

Table 1. Categorized a priori NO$_x$ emission rates in inversion region for two modeling episodes.

Modeling episodes	Area (tons day^{-1})	Mobile (tons day^{-1})	Non-road (tons day^{-1})	Biogenic (tons day^{-1})	Aircraft (tons day^{-1})	Lightning (tons day^{-1})	Elevated points (tons day^{-1})	Total (tons day^{-1})
Jun	453	760	374	474	172	434	543	3211
Aug–Sep	290	766	402	464	171	226	547	2866

Fig. 1. 12 km CAMx modeling domain for eastern Texas (black square), inversion regions (shaded), ground AQS NO$_2$ monitoring sites (blue triangles), and Moody Tower (red circle).

by the Global Biosphere Emissions and Interactions System (GloBEIS) biogenic emissions model, version 3.1 (Yarwood et al., 1999), with soil NO$_x$ emissions estimated by the Yienger and Levy method (Yienger and Levy, 1995).

Lightning and aircraft NO$_x$ emissions in the upper troposphere were missing in the base case emission inventories and should be added before conducting inversions. In this study, lightning NO emissions were developed based on National Lightning Detection Network (NLDN) data obtained from Vaisala Inc., following the approach of Kaynak et al. (2008). Intra-cloud lightning flashes were treated as three times the cloud-to-ground lightning flashes with 500 moles NO emission per flash. Lightning NO was placed into the model to match the time and location of NLDN flashes, and then distributed vertically based on the profile obtained from the mean April to September 2003–2005 vertical distribution of VHF sources from the Northern Alabama Lightning Mapping Array (Koshak et al., 2004). Global aircraft NO$_x$ emissions of year 2005 in 0.1° × 0.1° resolution were obtained from the Emis-

sion Database for Global Atmospheric Research (EDGAR) v4.1 (http://edgar.jrc.ec.europa.eu/datasets_grid_list41.php?v=41&edgar_compound=NOx), mapped to our modeling domain and placed at 9 km altitude.

2.3 Inversion regions

Five urban areas (Houston–Galveston–Brazoria (HGB), Dallas–Fort Worth (DFW), Beaumont–Port Arthur (BPA), northeast Texas (NE Texas), and Austin and San Antonio) plus two surrounding rural areas (north rural area (N rural) and south rural area (S rural)) (Fig. 1) were designed as inversion regions for the DKF inversions of NO$_x$ emissions. The five urban regions are all air quality planning areas included in Texas SIP development (Gonzales and Williamson, 2011). HGB and DFW were classified by US EPA as ozone nonattainment areas for violating the 1997 ozone National Ambient Air Quality Standard (NAAQS) of 84 ppb. BPA was designated as an ozone maintenance area, and NE Texas as well as Austin and San Antonio were designated as ozone early action compact areas under that standard. However, the recent tightening of the NAAQS to 75 ppb has heightened interest in ozone reduction in all of these regions. The sensitivities of NO$_2$ concentrations to boundary conditions and to NO$_x$ emissions from each inversion region and the border region (the area between model boundary and inversion regions) were computed through the decoupled direct method (DDM). The border region minimizes the impacts from boundary conditions on the inversion regions to the level of only 2 %. The DDM sensitivities show that NO$_x$ emissions from each urban region have the most impact on NO$_2$ concentrations within that region, and have less than 10 % influence on other regions.

2.4 Inversion method

Two methods were applied for inverse modeling: a direct scaling method introduced by Martin et al. (2003), and the DKF method. However, the direct scaling method creates spatial smearing errors when applied to regional models with fine resolution. It also assumes concentrations scale proportionally with emissions; hence, the nonlinearity between NO$_2$ concentrations and NO$_x$ emissions becomes problematic because NO$_x$ may influence its own lifetime by influencing concentrations of OH radicals (Martin et al., 2003). Thus, we present the direct scaling (DS) method and results
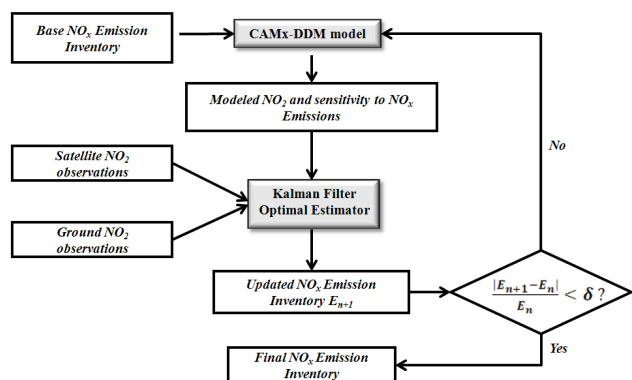
Fig. 2. Schematic diagram of Kalman filter inversion process.

in the Supplement (Sect. 3), and focus our attention on the DKF inversion.

The DKF inversion (Fig. 2) solves the spatial smearing problem by taking the spatial relationship between NO$_2$ concentrations and NO$_x$ emissions directly from model simulations, and also reduces the nonlinearity issue by performing the inversion iteratively. To constrain NO$_x$ emissions, the DKF inversion includes two processes at each time step: the measurement update (correction) process and the time update (prediction) process (Rodgers, 2000; Welch and Bishop, 2001). In the measurement update process at time step k (Eqs. 1–3), the inversion corrects the predicted NO$_x$ emission ($\mathbf{E}^-_{\mathrm{NO_x},k}$) and error covariance ($\mathbf{P}^-_{\mathrm{NO_x},k}$) by incorporating the measurement data ($\mathbf{C}^{\mathrm{measured}}_{\mathrm{NO_2},k}$) and Kalman gain ($\mathbf{G}_k$), and then generates the corrected emission ($\hat{\mathbf{E}}_{\mathrm{NO_x},k}$) and error covariance ($\hat{\mathbf{P}}_{\mathrm{NO_x},k}$).

$$\mathbf{G}_k = \mathbf{P}^-_{\mathrm{NO_x},k}\mathbf{S}_k^T(\mathbf{S}_k\mathbf{P}^-_{\mathrm{NO_x},k}\mathbf{S}_k^T + \mathbf{R}_k)^{-1} \tag{1}$$

$$\hat{\mathbf{E}}_{\mathrm{NO_x},k} = \mathbf{E}^-_{\mathrm{NO_x},k} + \mathbf{G}_k(\mathbf{C}^{\mathrm{measured}}_{\mathrm{NO_2},k} - \mathbf{C}^{\mathrm{modeled}}_{\mathrm{NO_2},k}) \tag{2}$$

$$\hat{\mathbf{P}}_{\mathrm{NO_x},k} = (\mathbf{I} - \mathbf{G}_k\mathbf{S}_k)\mathbf{P}^-_{\mathrm{NO_x},k} \tag{3}$$

$\mathbf{S}$ represents the NO$_2$ sensitivity to NO$_x$ emissions. $\mathbf{R}$ is the measurement error covariance, and it relates to the uncertainties in OMI and ground NO$_2$ measurements. In here, the uncertainty for the AQS ground NO$_2$ measurements was set to 0.15 (US EPA, 2006) and for the NASA standard OMI NO$_2$, version 2, was set to 0.3 (Bucsela et al., 2013) for all diagonal elements in $\mathbf{R}$. The error covariance ($\mathbf{P}$) relates to the uncertainty in the NO$_x$ emission inventory, and the uncertainty value of 2.0 (Napelenok et al., 2008) was chosen here for all diagonal elements in $\mathbf{P}$. To simplify, off-diagonal elements in $\mathbf{R}$ and $\mathbf{P}$ were set to zero, because we assume each inversion region is an independent element.

In the time update process at time step k, the inversion process predicts the emission ($\mathbf{E}^-_{\mathrm{NO_x},k+1}$) and the error covariance ($\mathbf{P}^-_{\mathrm{NO_x},k+1}$) for the measurement update process at time step $k+1$, based on the corrected emission ($\hat{\mathbf{E}}_{\mathrm{NO_x},k}$) and error covariance ($\hat{\mathbf{P}}_{\mathrm{NO_x},k}$) from the measurement update

process at time step k (Eqs. 4–5).

$$\mathbf{E}^-_{\mathrm{NO_x},k+1} = \mathbf{M}_k\hat{\mathbf{E}}_{\mathrm{NO_x},k} + \boldsymbol{\varepsilon}_k \tag{4}$$

$$\mathbf{P}^-_{\mathrm{NO_x},k+1} = \mathbf{M}_k\hat{\mathbf{P}}_{\mathrm{NO_x},k}\mathbf{M}_k^T + \mathbf{Q}_k \tag{5}$$

$\mathbf{M}$ represents a transition matrix; $\boldsymbol{\varepsilon}$ and $\mathbf{Q}$ are process errors which relate to errors in modeling processes, and are difficult to estimate. Since we assume the bias between modeled and measured NO$_2$ is mostly from errors in NO$_x$ emissions (Prinn, 2000; Napelenok et al., 2008), $\boldsymbol{\varepsilon}$ and $\mathbf{Q}$ were set to zero.

CAMx-DDM (Koo et al., 2007) calculates a semi-normalized NO$_2$ sensitivity to NO$_x$ emissions (unitless), as shown in Eq. (6), replacing sensitivity elements in $\mathbf{S}$ in Eq. (1),

$$S_{\mathrm{NO_2\,to\,NO_x}} = \tilde{E}_{\mathrm{NO_x}}\frac{\partial C_{\mathrm{NO_2}}}{\partial E_{\mathrm{NO_x}}} = \tilde{E}_{\mathrm{NO_x}}\frac{\partial C_{\mathrm{NO_2}}}{\partial((1+x)\tilde{E}_{\mathrm{NO_x}})} = \frac{\partial C_{\mathrm{NO_2}}}{\partial(1+x)} = \frac{\partial C_{\mathrm{NO_2}}}{\partial x}, \tag{6}$$

where $\tilde{E}$ represents the unperturbed NO$_x$ emission field; x is the perturbation factor. Hence, in this study, the DKF inversion actually seeks the optimal perturbation factor (x) at each iteration. The inversion processes will repeat iteratively until the perturbation factor for each emission region converges within a prescribed criterion, δ (Fig. 2), for which the value of 0.01 was chosen in this study.

2.5 NO$_2$ observations

2.5.1 Satellite NO$_2$ measurements

The Dutch-Finnish OMI aboard NASA's EOS Aura satellite, launched on 15 July 2004, is a nadir-viewing UV–vis spectrometer that measures solar backscattered irradiance in the range of 270 nm to 500 nm. It has been utilized to retrieve atmospheric NO$_2$ in the spectral range from 405 nm to 465 nm with spatial resolution down to scales of 13×24 km^2 at nadir view point (Levelt et al., 2006a, b). The EOS Aura satellite follows a Sun-synchronous polar orbit at approximately 705 km altitude with local Equator-crossing time around 13:40 (Levelt et al., 2006b; Boersma et al., 2007). In this study, the NASA standard product, version 2 (Bucsela et al., 2013) retrieval of OMI NO$_2$, gridded at $0.1° \times 0.1°$ resolution, was obtained from NASA Goddard Space Flight Center and mapped to the 12 km CAMx modeling domain. OMI pixels with cloud radiance fraction greater than 0.5 and sizes of more than 20×63 km^2 at swath edges were excluded in the dataset. The OMI averaging kernels (Eskes and Boersma, 2003) were interpolated into each CAMx model layer and then applied to the modeled NO$_2$ column density (Eq. 7), to account for the influence of the a priori NO$_2$ vertical profile used in the OMI retrieval and the OMI measurement sensitivities at each altitude:

$$C^{\mathrm{modeled}}_{\mathrm{NO_2}} = \sum A_i * X_i, \tag{7}$$

where A_i is the averaging kernel at pressure level i, and X_i is the CAMx-modeled partial NO$_2$ subcolumn density at the corresponding pressure level.

Table 2. Scaling factors for each region from different inversions.

Source region	3 June to 1 July 2006				16 August to 15 September 2006			
	Base NO$_x$ emission (tons day^{-1})	Priori NO$_x$ emission[a] (tons day^{-1})	Scaling factor relative to priori (unitless)		Base NO$_x$ emission (tons day^{-1})	Priori NO$_x$ emission (tons day^{-1})	Scaling factor relative to priori (unitless)	
			Posteriori OMI-based DKF inversion	Posteriori ground-based DKF inversion[b]			Posteriori OMI-based DKF inversion	Posteriori ground-based DKF inversion
HGB	374	455	1.12	0.36	382	436	1.03	0.54
DFW	335	435	1.02	0.33	314	412	1.14	0.46
BPA	81	97	1.83	0.47	86	98	1.75	0.40
NE Texas	141	164	1.84	0.47	155	174	0.56	0.47
Austin and San Antonio	252	319	1.28	0.29	248	302	1.70	0.38
N rural	522	823	1.67	–	543	759	1.98	–
S rural	472	728	1.52	–	489	668	1.72	–

[a] Adds lightning and aircraft NO$_x$ and doubled soil NO$_x$ emissions to the base case
[b] Conducted with 24 h averaged ground-level NO$_2$ data.

Table 3. Performance of CAMx in simulating OMI-observed NO$_2$ column densities.

Statistical parameters	3 June to 1 July 2006			16 August to 15 September 2006		
	Base case	Priori[c]	Posteriori OMI-based DKF inversion	Base case	Priori	Posteriori OMI-based DKF inversion
R^2	0.62	0.61	0.54	0.63	0.48	0.51
NMB[a]	−0.47	−0.30	−0.12	−0.54	−0.33	−0.12
NME[b]	0.48	0.32	0.23	0.55	0.39	0.28

[a] Normalized mean bias
[b] Normalized mean error
[c] Adds lightning and aircraft NO$_x$ and doubled soil NO$_x$ emissions to the base case.

In order to reduce the OMI measurement uncertainties and effects from invalid data points, monthly averaged OMI NO$_2$ column densities were used in the DKF inversions.

2.5.2 Ground and other NO$_2$ measurements

The US EPA Air Quality System (AQS) NO$_2$ ground monitoring network data (Fig. 1) (http://www.epa.gov/ttn/airs/airsaqs/) were also used for inverse modeling. AQS monitors are equipped with a heated molybdenum catalytic converter that first transforms NO$_2$ to NO, and then measures the resultant NO using a chemiluminescence analyzer. NO$_2$ is then calculated by subtracting NO measured in a separate NO mode from the resultant NO (US EPA, 1975). Studies (US EPA, 1975; Demerjian, 2000; Lamsal et al., 2008) indicate that the catalytic converter also converts fractions of other reactive nitrogen species (e.g. HNO$_3$, PAN) into NO during this measurement. Therefore, correction factors computed from CAMx-modeled concentrations by the method of Lamsal et al. (2008) (Eq. 8) are applied before deploying the AQS NO$_2$ data in the DKF inversion:

$$CF = \frac{NO_2}{NO_2 + \sum AN + (0.95PAN) + (0.35HNO_3)}. \quad (8)$$

In Eq. (8), $\sum$AN represents the sum of all alkyl nitrates and PAN is peroxyacetyl nitrate. The CAMx model with CB05 mechanism does not output alkyl nitrates specifically, so the difference between modeled total organic nitrates and PAN was used to represent modeled alkyl nitrates.

The NOAA P-3 aircraft NO$_2$ data (http://www.esrl.noaa.gov/csd/tropchem/2006TexAQS/) and the Texas Radical and Aerosol Measurement Program (TRAMP) NO$_2$ data, measured at Moody Tower (Fig. 1), (http://geossun2.geosc.uh.edu/web/blefer/TRAMP/Final%20data/) were used to evaluate the inverse modeling results. The Moody Tower measurement site located at the University of Houston campus is approximately 70 m above the ground (Luke et al., 2010), corresponding to the CAMx modeling layer 2, with hourly NO$_2$ data available for the whole August–September episode, but no coverage for the June episode. The P-3 aircraft measurement was made from ground level to around 5000 m height with 1 s resolution, but only available on 4 days (31 August, 11 September, 13 September, and 15 September 2006) during our modeling period. Hourly averaged aircraft NO$_2$ data were used to compare with the hourly modeled NO$_2$ at corresponding grid cells. Both P-3 aircraft and Moody Tower

Table 4. Performance of CAMx in simulating AQS ground-level NO$_2^*$.

Statistical parameters	3 June to 1 July 2006				16 August to 15 September 2006			
	Base case	Priori	Posteriori OMI-based DKF inversion	Posteriori ground-based DKF inversion	Base case	Priori	Posteriori OMI-based DKF inversion	Posteriori ground-based DKF inversion
R^2	0.56	0.56	0.53	0.54	0.52	0.52	0.46	0.49
NMB	0.89	0.98	1.39	−0.16	0.42	0.49	0.81	−0.23
NME	1.01	1.09	1.45	0.47	0.66	0.71	0.96	0.48

* Hourly AQS data were used to compare with modeled NO$_2$ at corresponding locations.

Table 5. Performance of CAMx in simulating P-3 aircraft-observed NO$_2$ and NO$_y$.

Statistical parameters	NO$_2^*$				NO$_y^*$			
	Base case	Priori	Posteriori OMI-based DKF inversion	Posteriori ground-based DKF inversion	Base case	Priori	Posteriori OMI-based DKF inversion	Posteriori ground-based DKF inversion
R^2	0.23	0.23	0.22	0.21	0.34	0.34	0.37	0.30
NMB	0.10	0.10	0.15	−0.15	0.65	0.68	0.84	0.46
NME	0.99	0.99	1.01	0.85	0.94	0.97	1.08	0.83

* Comparison available for only four days (31 August, 11, 13, and 15 September 2006).

NO$_2$ measurements were made by using a photolytic converter, and hence did not require corrections via Eq. (8).

3 Results and discussion

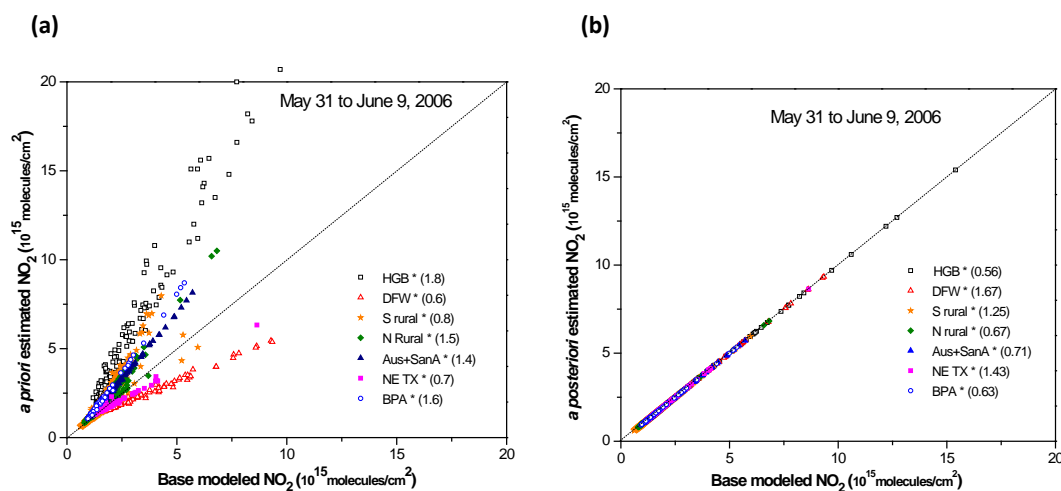### 3.1 Pseudodata test for the DKF inversion with CAMx-DDM

To evaluate the performance of the DKF inversion technique, a controlled pseudodata test was performed for 10 modeling days (31 May to 9 June, and 13 to 22 August) for each modeling episode. The 10-day averaged modeled NO$_2$ columns at 13:00–14:00 LT from the base case were used as pseudo-observations, and the model was rerun with NO$_x$ emissions from each region perturbed by known factors ranging from 0.5 to 2.0 (Fig. 3). Applying the DKF inversion successfully adjusted the perturbed NO$_x$ emissions from each region back to their base values, converging in 4 iterations (Fig. 3). The robustness of the DKF inversion was tested by varying the uncertainty parameters, which were set to 2.0 for emissions and 0.3 for observations in the initial pseudodata test. While higher levels of the emission uncertainty parameter and lower levels of the observation uncertainty parameter led to more rapid adjustments, the final results of the DKF inversion were insensitive to the assumed uncertainty parameters, and also to the off-diagonal elements in the error covariance matrix. Similar results were found by adjusting the assumed uncertainty parameters and error covariance matrix in the actual simulations (Supplement Fig. S3).

3.2 Additional NO$_x$ emissions

Since DKF inversions scale emissions from their original levels, an appropriate a priori NO$_x$ emission inventory is essential for obtaining reasonable results. The NASA Intercontinental Chemical Transport Experiment (INTEX-A) air quality study (Singh et al., 2006) found large discrepancies between aircraft measurements and CMAQ simulations of NO$_2$ concentrations in the upper troposphere. Possible explanations could be upper tropospheric NO$_x$ sources, such as lightning and aircraft NO$_x$ emissions, that are often neglected in emission inventories. Missing NO$_x$ sources in the upper troposphere may bias the inversion on the remaining emissions (Napelenok et al., 2008). At ground level, Hudman et al. (2010) found that the soil NO$_x$ emissions estimated by the widely used Yienger and Levy method (Yienger and Levy, 1995) were underestimated by a factor of 2 over the United States. Therefore, in this study, the lightning and aircraft NO$_x$ emissions were added in the upper troposphere as described in the Sect. 2.2, and the soil NO$_x$ emissions were doubled from base case levels (Table 1). The emission inventory with added lightning and aircraft NO$_x$ and doubled soil NO$_x$ (hereafter referred to as the a priori emission inventory) was used for the following inversion studies. Inclusion of these NO$_x$ sources improves the performance of the model in simulating satellite-observed NO$_2$ column densities, especially in the rural areas (Figs. 4c and 5c), and reduces the bias and error by around 15 % (Table 3).

Table 6. Performance of CAMx in simulating AQS hourly ground-level O$_3$.

Statistical parameters	3 June to 1 July 2006			16 August to 15 September 2006		
	Priori	Posteriori OMI-based DKF inversion	Posteriori ground-based DKF inversion	Priori	Posteriori OMI-based DKF inversion	Posteriori ground-based DKF inversion
R^2	0.61	0.63	0.57	0.50	0.51	0.46
NMB	0.01	0.02	0.04	0.38	0.41	0.40
NME	0.29	0.30	0.30	0.47	0.50	0.48

Fig. 3. Pseudodata test showing that the DKF inversion accurately adjusts the NO$_x$ emissions from the perturbed case **(a)** to the a posteriori case **(b)** to match the desired base NO$_2$ column densities. Numbers indicate perturbation factors in the legend **(a)** and adjustment factors in the legend **(b)**. Similar performance is found for the 13–22 August test period.

3.3 Top-down NO$_x$ emissions using OMI NO$_2$

DKF inversion using the OMI NO$_2$ measurements was conducted to constrain NO$_x$ emissions from the seven designated regions. The monthly averaged (3 June to 1 July and 16 August to 15 September) OMI and CAMx NO$_2$ column densities at 13:00–14:00 were used in the inversion. All modeling grids in the inversion area were covered by the OMI NO$_2$ measurement data. The DKF inversions were performed with 2116 data points in one time step (13:00–14:00). The scaling factors generated by inversion for each region were applied to the NO$_x$ emission inventory hourly, since we assume that the 13:00–14:00 NO$_2$ column density is contributed by the NO$_x$ emissions from all previous hours, and the uncertainty in the bottom-up NO$_x$ emission inventory should be the same for every time step. The satellite-based DKF inversions scale a priori NO$_x$ emissions by factors ranging from 1.02 to 1.84 in almost all regions in both episodes (Table 2), adhering to the specified uncertainty range of 0.5 to 2.0 (Hanna et al., 2001). The scaling factors tend to be larger over the rural and small urban regions than over the urban DFW and HGB ozone nonattainment regions, where the inversions scale up emissions only slightly (factors of 1.02 to 1.14). It results from

the inversion attempts to compensate for the large gap between higher observed than modeled NO$_2$ over rural regions, despite varied patterns over urban grid cells. One exception occurs in the NE Texas region in the August–September episode (Table 2), which shows downward scaling (factor of 0.56). This reflects the inversion shifting emissions between NE Texas and the much larger surrounding N rural region (Fig. 1); taken together, the net scaling factor for the two regions in the August–September episode is 1.72, consistent with the upward scaling of rural emissions throughout the two episodes. Apart from this anomaly, scaling factors for most regions were consistent across the two episodes, varying by less than 15 %.

CAMx-modeled NO$_2$ column densities with the inverted NO$_x$ emissions (Figs. 4d and 5d) are increased by 3–55 % in all regions, but the increments are much more moderate compared to the DS method inversion (Fig. S4). The statistical results (Table 3) indicate that the DKF inversed NO$_2$ are closer to OMI observations than the a priori case in terms of 20 % less in bias and 10 % less in error, but without improvements in the spatial distribution. The DS method scales up NO$_x$ emissions more than the DKF inversion (Table S2), making the inversed NO$_2$ concentrations have slightly less
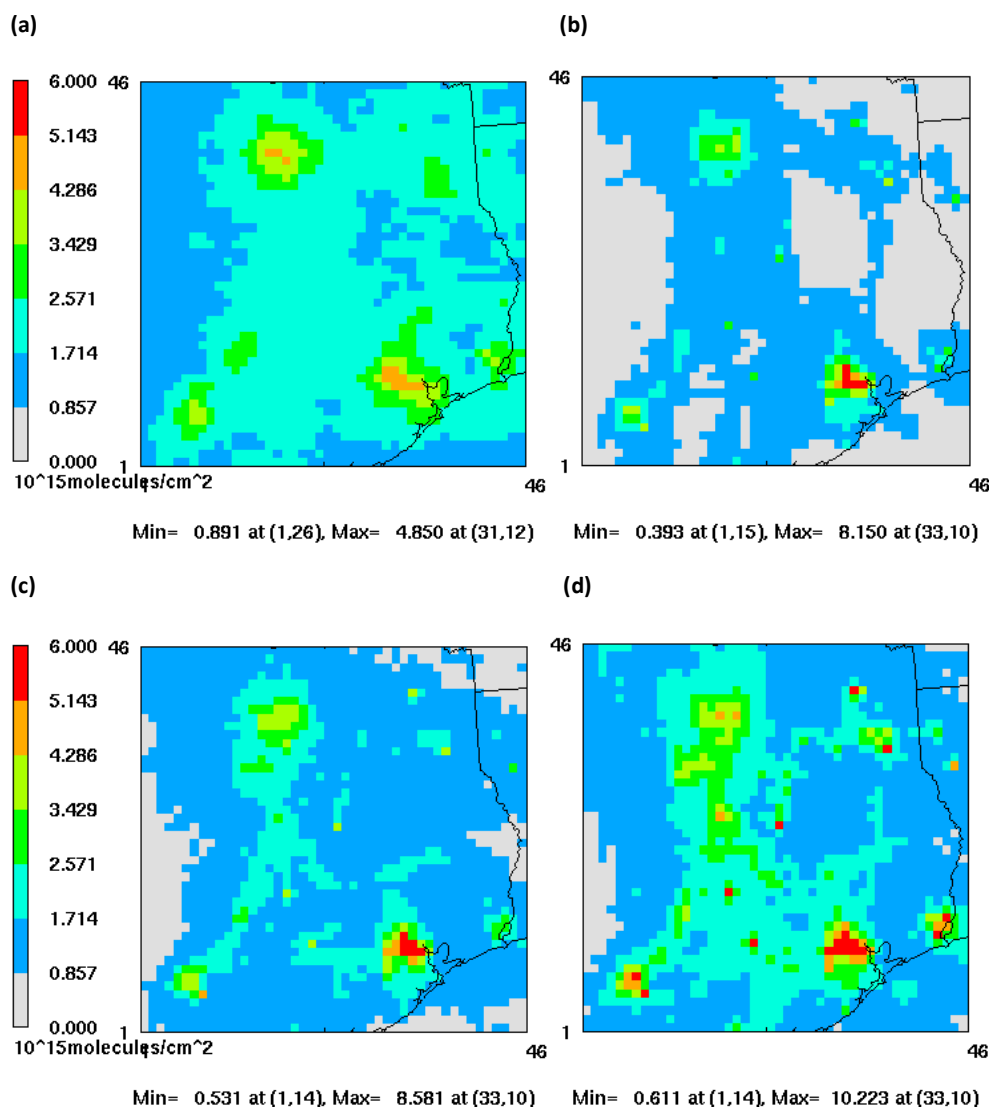
(a)

Min= 0.891 at (1,26), Max= 4.850 at (31,12)

(b)

Min= 0.393 at (1,15), Max= 8.150 at (33,10)

(c)

Min= 0.531 at (1,14), Max= 8.581 at (33,10)

(d)

Min= 0.611 at (1,14), Max= 10.223 at (33,10)

Fig. 4. Monthly averaged (3 June to 1 July) tropospheric NO$_2$ vertical columns at 13:00–14:00 from **(a)** OMI observations, and from CAMx simulations using **(b)** base case emission inventory, **(c)** a priori emission inventory (with additional lightning, aircraft, and soil NO$_x$), and OMI-based inverted NO$_x$ emissions using **(d)** the DKF method.

bias and error (Table S3). However, the DKF inverse NO$_2$ has better R^2 than the DS method, indicating the DKF inversion method has better ability to retain the spatial structure of NO$_x$ emissions. Each of the inversions using OMI NO$_2$ data actually worsens the model performance in simulating ground-level NO$_2$ concentrations (Table 4), since the modeled ground NO$_2$ using the base case emission inventory had already been overestimated (Fig. 6). Similarly, since the base model already overestimated P-3 aircraft observations of NO$_2$ and NO$_y$, the DKF inversion worsens model bias relative to these measurements (Table 5). Greater deterioration resulted from the DS inversion (Tables S3–S6).

3.4 Top-down NO$_x$ emissions using ground AQS NO$_2$

Ground-level AQS NO$_2$ measurements were also used to drive DKF inversions of NO$_x$ emissions for the two modeling episodes. There are 37 ground measurement sites in the designated inversion regions (Fig. 1), mostly located in the urban cores. The N rural and S rural regions were excluded in this case because they contain too few measurement sites. Correction factors from Eq. (8) were applied to the ground NO$_2$ before using the data in the inversion.

The base case simulations strongly overpredicted observed NO$_2$ in the early morning and late afternoon during both modeling episodes (Fig. 6), when the model may underestimate PBL heights (Kolling et al., 2013). To alleviate the
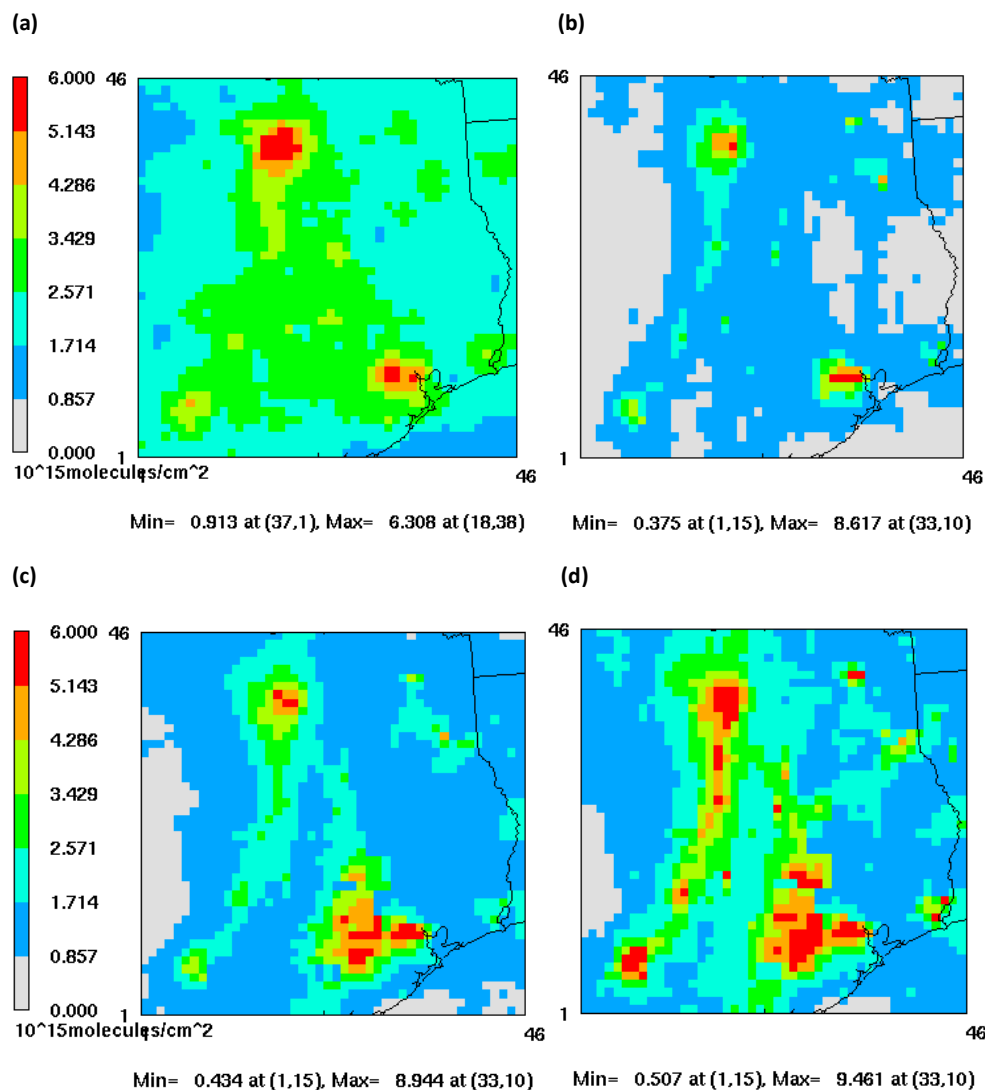
Fig. 5. Same as Fig. 4, but for the August–September episode.

influence from PBL heights, daily 24 h averaged NO$_2$ levels were used in the inversions.

To address the overprediction of ground-level NO$_2$, the ground-based inversions sharply reduce a priori NO$_x$ emissions by applying scaling factors of 0.30 to 0.57 (Table 2). The reductions in NO$_x$ emissions reduce model error relative to the AQS (Table 4) and Moody Tower NO$_2$ observations on an hourly basis, as well as NO$_2$ and NO$_y$ observed by the P-3 aircraft (Table 5), but may be too sharp, as they lead negative bias in predicting NO$_2$ from the AQS monitors (Table 4) and the P-3 aircraft NO$_2$ measurements (Table 5). More moderate scaling factors are obtained if the inversion is conducted with data only from a midday window (9:00–14:00) when PBL heights are less problematic (not shown). However, scaling factors still remain far below 1.0 and show up to factor-of-two inconsistencies between the two episodes.

3.5　Impacts on O$_3$ simulations

O$_3$ concentrations and their sensitivities to changes in emissions are calculated for both modeling episodes using the a priori and each of the a posteriori emission inventories. The scaled-up NO$_x$ emissions from the satellite-based DKF inversion (Table 2) lead to 1–7 ppb higher modeled 8 h (10:00–18:00) O$_3$ concentrations over most of the domain in the June episode (Fig. 7, top row). Largest increases occur over NE Texas and N rural regions (Fig. 1), where the a priori simulation shows O$_3$ to be most sensitive to NO$_x$ (Fig. 7, middle row) and where the satellite-based DKF inversion scaled up emissions by large amounts.

The a priori simulation shows O$_3$ to be primarily sensitive to NO$_x$ over most of the domain, but VOC-limited in the core of the Houston region and with joint sensitivity to NO$_x$ and VOC in Dallas, Austin, and San Antonio (Fig. 7, left
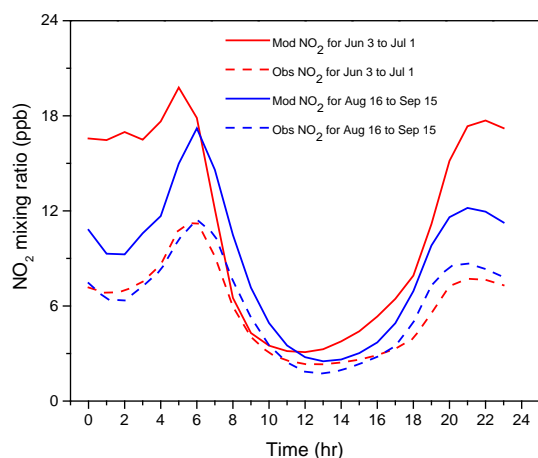
Fig. 6. Daily variations of modeled (solid line) and observed (dashed line) ground NO$_2$ concentrations for the June (red) and August–September (blue) episodes. Note: NO$_2$ concentrations were taken by averaging monthly data for all sites.

column). The satellite-based inversion increases NO$_x$ emissions and thus shifts the O$_3$ formation chemistry toward being more VOC sensitive (Fig. 7, middle column). Over much of the domain, O$_3$ sensitivity to VOC increases by a factor of about 1.5. The slight increases in O$_3$ sensitivity to NO$_x$ occur because the semi-normalized sensitivity coefficients represent the local slope of O$_3$-emission response scaled to a 100 % change in emissions. As the satellite-based inversion scales up NO$_x$ emissions, these semi-normalized coefficients increase, even though the impacts per ton of NO$_x$ decrease.

The ground-based DKF inversion leads to O$_3$ reductions of 3–8 ppb over urban regions (Fig. 7, top right), where it scales down emissions (Table 2), and less changes over rural regions, where emissions were left unchanged due to lack of NO$_2$ monitors. The reduction in urban NO$_x$ makes O$_3$ less sensitive to VOC emissions as expected (Fig. 7, bottom right). However, the impact on sensitivity to NO$_x$ is mixed. In urban areas which are transitional between NO$_x$-limited and NO$_x$-saturated conditions, the reduction in NO$_x$ emissions pushes the chemistry toward more NO$_x$-limited conditions and thus increases the sensitivities. In downwind regions which are already NO$_x$-limited, the sensitivities decline because there are now less NO$_x$ emissions contributing to the semi-normalized coefficients.

Model performance in simulating hourly AQS ground-level observations of O$_3$ indicates that the bias and error slightly worsened when each of the a posteriori inventories are used in place of the a priori inventory (Table 6). The largest deterioration comes from the DS inversion as the bias and error increase by around 10 % (Table S5), likely because this inversion method does not retain the spatial structure of emissions from the a priori inventory. For the other inversions, the changes in bias and error are too slight to determine if performance is meaningfully impacted.

4 Conclusions

Inverse modeling has been performed using either NO$_2$ column densities observed by OMI satellite or ground-level NO$_2$ concentrations observed by AQS monitors to constrain the NO$_x$ emissions for two regulatory attainment modeling episodes in Texas. Two inversion methods, DS and DKF, are applied to the OMI NO$_2$ data, and the DKF method is also applied to the ground-level NO$_2$ data. Pseudodata test results validate that the DKF method effectively captures known perturbations in CAMx simulations.

Two missing NO$_x$ sources in the upper troposphere, lightning and aircraft NO$_x$ emissions, are added into the base case NO$_x$ emission inventory, contributing 14 % and 6 % to the total NO$_x$ emissions for the June episode, and 7 % and 6 % for the August–September episode, respectively. The underestimated soil NO$_x$ emissions are doubled from the base case, adding an additional 8 % NO$_x$ emission to the base case for both episodes. The additional NO$_x$ emissions increase the modeled NO$_2$ column densities mostly at rural areas and improve the inversion performance with the OMI NO$_2$, but not with the ground NO$_2$.

The DS method was originally pursued to provide an alternate approach featuring more spatial heterogeneous adjustments to emissions. However, it tends to overshoot the OMI-observed NO$_2$ column densities since this linear inversion method ignores the nonlinear influence of NO$_x$ on its own lifetime. The iterative approach of the DKF inversion avoids this problem, but fails to substantially improve the spatial correlation of modeled and observed NO$_2$ levels since it applies only a single scaling factor to each inversion region.

The overall tendency of the model to underpredict OMI-observed NO$_2$ column densities and to overpredict AQS-observed ground NO$_2$ concentrations leads to conflicting results between the inversions. It is difficult to determine which observations provide a more reliable basis for the inversions, since none of the inversions improve model performance against independent data such as aircraft-observed NO$_2$ or ground-level O$_3$ concentrations. Whether this indicates that the a priori inventory is the best available representation of NO$_x$ emissions, or that tuning of the base model led to its better performance, is impossible to determine. Nevertheless, this suggests that inverse modeling of NO$_x$ emissions should for now remain a complement to SIP modeling efforts rather than a substitute for traditional bottom-up inventories.

The AQS ground NO$_2$ measurements face limitations due to the inaccuracies of the molybdenum converter method. Furthermore, the mostly urban locations of measurement sites may be unrepresentative of the entire region, and do not capture the rural areas where OMI observations suggest NO$_2$ is underestimated. In addition, model shortcomings in simulating PBL heights in the early morning and late afternoon may contribute to the low scaling factors in the ground-based inversions.
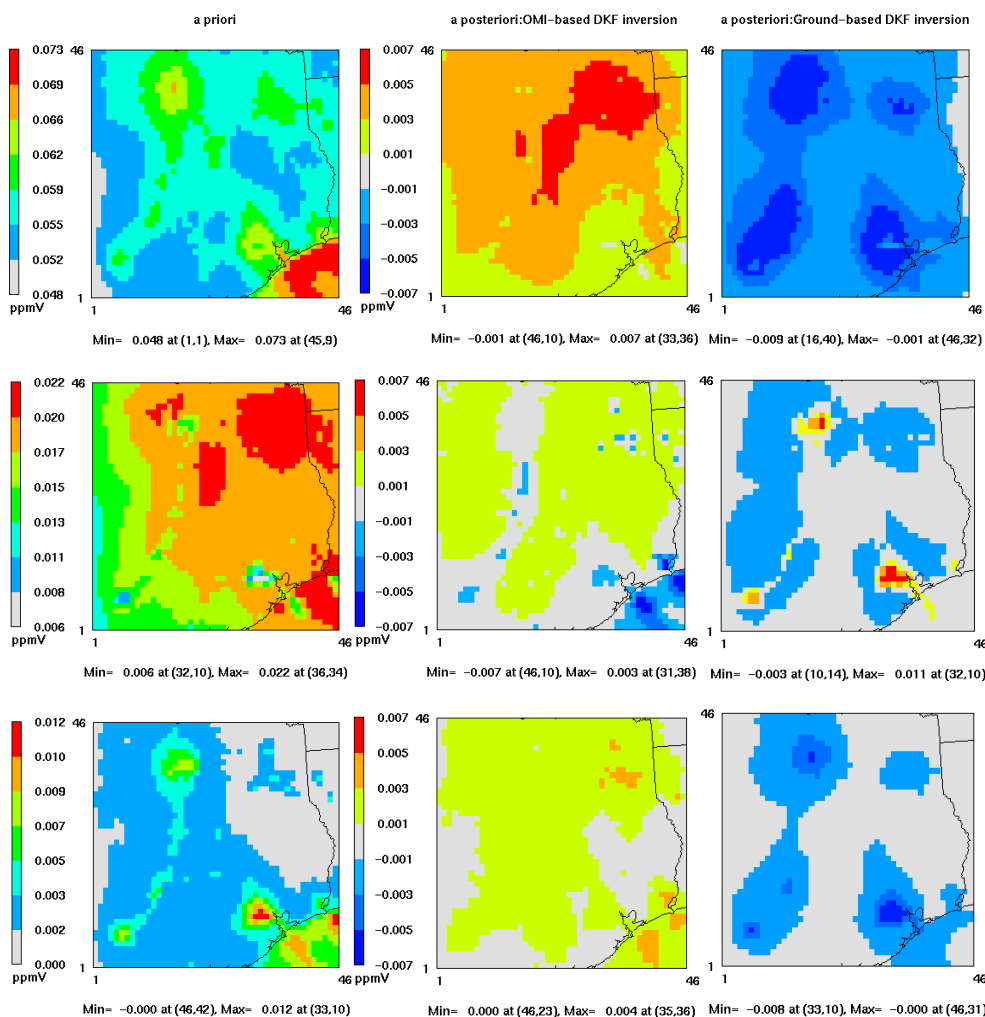
Fig. 7. Monthly 8 h (10:00–18:00) averaged ground-level O$_3$ concentrations (top), O$_3$ sensitivity to NO$_x$ (middle), and O$_3$ sensitivity to VOC (bottom) for the a priori case (left column), and differences (a posteriori minus a priori) for the OMI-based (middle column) and ground-based (right column) DKF inversions in the June episode. The August–September episode shows similar results.

For the satellite data, several factors could explain the more spatially smeared and higher rural NO$_2$ in the satellite observations than the base model which drove the upward scaling of emissions. Our inclusion of lightning and aircraft NO$_x$ emissions and doubling of soil NO$_x$ emissions narrowed but did not eliminate the discrepancy. A higher-resolution OMI NO$_2$ product (retrieved with small pixels and high-resolution a priori profile) has been shown to enhance NO$_2$ column densities in urban areas and reduce them in rural areas (Russell et al., 2011), which would more closely resemble the modeled distribution. Lin et al. (2012) highlighted several uncertain model parameterizations that impact model predictions of NO$_2$ column density for a given emission inventory. For example, lowering the rate constant of the NO$_2$ + OH reaction to match the rate of Mollner et al. (2010) would lead to a longer NO$_x$ lifetime and reduce the gap between modeled urban and rural NO$_2$ concentrations.

Henderson et al. (2011) suggested that better representation of acetone and organic nitrates in the CB05 mechanism could help address its underprediction of NO$_2$ in the remote upper troposphere. Future work could explore how combinations of these adjustments influence satellite-based inversions.

The DISCOVER-AQ campaign by NASA in fall 2013 will provide vertically resolved measurements of NO$_x$ from repeated aircraft spirals in the Houston region. This may help resolve some of the discrepancies noted here between inversions driven by ground-based and satellite-based NO$_2$ observations. The future Tropospheric Emissions: Monitoring of Pollution (TEMPO) mission, using a geostationary satellite with high spatial and temporal measurement capabilities, could provide a richer data source to drive the NO$_x$ inversions. Future work could also conduct inversions based on emission categories rather than emission regions, to explore

potential errors in the emission inventory on a component rather than location basis.

Supplementary material related to this article is available online at http://www.atmos-chem-phys.net/13/11005/2013/acp-13-11005-2013-supplement.pdf.

References

Boersma, K. F., Eskes, H. J., Veefkind, J. P., Brinksma, E. J., van der A, R. J., Sneep, M., van den Oord, G. H. J., Levelt, P. F., Stammes, P., Gleason, J. F., and Bucsela, E. J.: Near-real time retrieval of tropospheric NO$_2$ from OMI, Atmos. Chem. Phys., 7, 2103–2118, doi:10.5194/acp-7-2103-2007, 2007.

Bovensmann, H., Burrows, J. P., Buchwitz, M., Frerick, J., Noël, S., Rozanov, V. V., Chance, K. V., and Goede, A. P. H.: SCIA-MACHY: Mission Objectives and Measurement Modes, J. Atmos. Sci., 56, 127–150, 1999.

Brioude, J., Kim, S. W., Angevine, W. M., Frost, G. J., Lee, S. H., McKeen, S. A., Trainer, M., Fehsenfeld, F. C., Holloway, J. S., Ryerson, T. B., Williams, E. J., Petron, G., and Fast, J. D.: Top-down estimate of anthropogenic emission inventories and their interannual variability in Houston using a mesoscale inverse modeling technique. J. Geophys. Res., 116, D20305, doi:10.1029/2011JD016215, 2011.

Bucsela, E. J., Krotkov, N. A., Celarier, E. A., Lamsal, L. N., Swartz, W. H., Bhartia, P. K., Boersma, K. F., Veefkind, J. P., Gleason, J. F., and Pickering, K. E.: A new stratospheric and tropospheric NO$_2$ retrieval algorithm for nadir-viewing satellite instruments: applications to OMI, Atmos. Meas. Tech., 6, 2607–2626, doi:10.5194/amt-6-2607-2013, 2013.

Chai, T., Carmichael, G. R., Tang, Y., Sandu, A., Heckel, A., Richter, A., and Burrows, J. P.: Regional NO$_x$ emission inversion through a four-dimensional variational approach using SCIA-MACHY tropospheric NO$_2$ column observations. Atmos. Environ., 43, 5046–5055, 2009.

Chang, M. E., Hartley, D. E., Cardelino, C., and Chang, W. L.: Inverse modeling of biogenic isoprene emissions. Geophys. Res. Lett., 23, 3007–3010, 1996.

Deguillaume, L., Beekmann, M., and Menut, L.: Bayesian Monte Carlo analysis applied to regional-scale inverse emission modeling for reactive trace gases. J. Geophys. Res., 112, D02307, doi:10.1029/2006JD007518, 2007.

Demerjian, K. L.: A review of national monitoring networks in North America. Atmos. Environ., 34, 1861–1884, 2000.

ENVIRON: User's Guide to Emissions Processor, Version 3. ENVIRON International Corporation, Novato, CA, USA, 2007.

ENVIRON: Boundary Conditions and Fire Emissions Modeling, Final Report to the Texas Commission on Environmental Quality. ENVIRON International Corporation, Novato, CA, USA, 2008.

ENVIRON: CAMx Users' Guide, version 5.30. ENVIRON International Corporation, Novato, CA, USA, 2010.

Eskes, H. J. and Boersma, K. F.: Averaging kernels for DOAS total-column satellite retrievals, Atmos. Chem. Phys., 3, 1285–1291, doi:10.5194/acp-3-1285-2003, 2003.

Gilliland, A. B. and Abbitt, P. J.: A sensitivity study of the discrete Kalman filter (DKF) to initial condition discrepancies, J. Geophys. Res., 106, 17939–17952, 2001.

Gilliland, A. B., Dennis, R. L., Roselle, S. J., and Pierce, T. E.: Seasonal NH$_3$ emission estimates for the eastern United States based on ammonium wet concentrations and an inverse modeling method, J. Geophys. Res., 108, 4477, doi:10.1029/2002JD003063, 2003.

Gonzales, M. and Williamson, W.: Updates on the National Ambient Air Quality Standards and the State Implementation Plans for Texas. Presented at TCEQ Trade Fair, TX. May 2011.

Grell, G. A., Dudhia, J., and Stauffer, D.: A description of the fifth-generation PennState/NCAR mesoscale model (MM5), NCAR Technical Note, NCAR/TN 398 + SR, 1994.

Haas-Laursen, D. E., Hartley, D. E., and Prinn, R. G.: Optimizing an inverse method to deduce time-varying emissions of trace gases. J. Geophys. Res., 101, 22823–22831, 1996.

Hanna, S. R., Lu, Z., Frey, H. C., Wheeler, N., Vukovich, J., Arumachalam, S., and Fernau, M.: Uncertainties in predicted ozone concentration due to input uncertainties for the UAM-V photochemical grid model applied to the July 1995 OTAG domain, Atmos. Environ., 35, 891–903, 2001.

Henderson, B. H., Pinder, R. W., Crooks, J., Cohen, R. C., Hutzell, W. T., Sarwar, G., Goliff, W. S., Stockwell, W. R., Fahr, A., Mathur, R., Carlton, A. G., and Vizuete, W.: Evaluation of simulated photochemical partitioning of oxidized nitrogen in the upper troposphere, Atmos. Chem. Phys., 11, 275–291, doi:10.5194/acp-11-275-2011, 2011.

Hudman, R. C., Russell, A. R., Valin, L. C., and Cohen, R. C.: Inter-annual variability in soil nitric oxide emissions over the United States as viewed from space, Atmos. Chem. Phys., 10, 9943–9952, doi:10.5194/acp-10-9943-2010, 2010.

Jaeglé, L., Steinberger, L., Martin, R. V., and Chance, K.: Global partitioning of NO$_x$ sources using satellite observations: Relative roles of fossil fuel combustion, biomass burning and soil emissions, Faraday Discuss., 130, 407–423, 2005.

Kaynak, B., Hu, Y., Martin, R. V., Russell, A. G., Choi, Y., and Wang, Y.: The effect of lightning NOx production on surface ozone in the continental United States, Atmos. Chem. Phys., 8, 5151–5159, doi:10.5194/acp-8-5151-2008, 2008.

Kolling, J. S., Pleim, J. E., Jeffries, H. E., and Vizuete, W.: A multisensor evaluation of the Asymmetric Convective Model, Version 2, in Southeast Texas, J. Air Waste Manage., 63, 41–53, doi:10.1080/10962247.2012.732019, 2013.

Konovalov, I. B., Beekmann, M., Richter, A., and Burrows, J. P.: Inverse modelling of the spatial distribution of NOx emissions on a continental scale using satellite data, Atmos. Chem. Phys., 6, 1747–1770, doi:10.5194/acp-6-1747-2006, 2006.

Konovalov, I. B., Beekmann, M., Burrows, J. P., and Richter, A.: Satellite measurement based estimates of decadal changes in European nitrogen oxides emissions, Atmos. Chem. Phys., 8, 2623–2641, doi:10.5194/acp-8-2623-2008, 2008.

Koo, B., Yarwood, G., and Cohan, D. S: Incorporation of High-order Decoupled Direct Method (HDDM) Sensitivity Analysis Capability into CAMx, Prepared for Texas Commission on Environmental Quality, 2007.

Koshak, W. J., Solakiewicz, R. J., Blakeslee, R. J., Goodman, S. J., Christian, H. J., Hall, J. M., Bailey, J. C., Krider, E. P., Bateman, M. G., Boccippio, D. J., Mach, D. M., McCaul, E. W., Stewart, M. F., Buechler, D. E., Petersen, W. A., and Cecil, D. J.: North Alabama Lightning Mapping Array (LMA): VHF source retrieval algorithm and error analyses, J. Atmos. Ocean. Tech., 21, 543–558, 2004.

Kurokawa, J., Yumimoto, K., Uno, I., and Ohara, T.: Adjoint inverse modeling of NO$_x$ emissions over eastern China using satellite observations of NO$_2$ vertical column densities, Atmos. Environ., 43, 1878–1887, 2009.

Lamsal, L. N., Martin, R. V., van Donkelaar, A., Steinbacher, M., Celarier, E. A., Bucsela, E., Dunlea, E. J., and Pinto, J. P.: Ground level nitrogen dioxide concentrations inferred from the satellite borne Ozone Monitoring Instrument, J. Geophys. Res., 113, D16308, doi:10.1029/2007JD009235, 2008.

Levelt, P. F., Hilsenrath, E., Leppelmeier, G. W., van den Oord, G. H. J., Bhartia, P. K., Tamminen, J., de Haan, J. F., and Veefkind, J. P.: Science objective of the Ozone Monitoring Instrument. IEEE T. Geosci. Remote., 44, 1199–1208, 2006a.

Levelt, P. F., van den Oord, G. H. J., Dobber, M. R., Malkki, A., Visser, H., de Vries, J., Stammes, P., Lundell, J. O. V., and Saari, H.: The Ozone Monitoring Instrument, IEEE. T. Geosci. Remote., 44, 1093–1101, 2006b.

Lin, J.-T., McElroy, M. B., and Boersma, K. F.: Constraint of anthropogenic NO$_x$ emissions in China from different sectors: a new methodology using multiple satellite retrievals, Atmos. Chem. Phys., 10, 63–78, doi:10.5194/acp-10-63-2010, 2010.

Lin, J.-T., Liu, Z., Zhang, Q., Liu, H., Mao, J., and Zhuang, G.: Modeling uncertainties for tropospheric nitrogen dioxide columns affecting satellite-based inverse modeling of nitrogen oxides emissions, Atmos. Chem. Phys., 12, 12255–12275, doi:10.5194/acp-12-12255-2012, 2012.

Luke, W. T., Kelley, P., Lefer, B. L., Flynn, J., Rappenglück, B., Leuchner, M., Dibb, J. E., Ziemba, L. D., Anderson, C. H., and Buhr, M.: Measurements of primary trace gases and NO$_y$ composition in Houston, Texas, Atmos. Environ., 44, 4068–4080, 2010.

Martin, R. V., Jacob, D. J., Chance, K., Kurosu, T. P., Palmer, P. I., and Evans, M. J.: Global inventory of nitrogen oxide emissions constrained by space-based observations of NO$_2$ columns. J. Geophys. Res., 108, 4537, doi:10.1029/2003JD003453, 2003.

Mendoza-Dominguez, A. and Russell, A. G.: Iterative inverse modeling and direct sensitivity analysis of a photochemical air quality model, Environ. Sci. Technol., 34, 4974–4981, 2000.

Mollner, A. K., Valluvadasan, S., Feng, L., Sprague, M. K., Okumura, M., Milligan, D. B., Bloss, W. J., Sander, S. P., Martien, P. T., Harley, R. A., McCoy, A. B., and Carter, W. P. L.: Rate of gas phase association of hydroxyl radical and nitrogen dioxide. Science, 330, 646–649, doi:10.1126/science.1193030, 2010.

Mulholland, M. and Seinfeld, J. H.: Inverse air pollution modeling of urban-scale carbon monoxide emissions. Atmos. Environ., 29, 497–516, 1995.

Müller, J. F. and Stavrakou, T.: Inversion of CO and NO$_x$ emissions using the adjoint of the IMAGES model, Atmos. Chem. Phys., 5, 1157–1186, doi:10.5194/acp-5-1157-2005, 2005.

Napelenok, S. L., Pinder, R. W., Gilliland, A. B., and Martin, R. V.: A method for evaluating spatially-resolved NO$_x$ emissions using Kalman filter inversion, direct sensitivities, and space-based NO$_2$ observations, Atmos. Chem. Phys., 8, 5603–5614, doi:10.5194/acp-8-5603-2008, 2008.

Pison, I., Menut, L., and Bergametti, G.: Inverse modeling of surface NO$_x$ anthropogenic emission fluxes in the Paris area during the Air Pollution Over Paris Region (ESQUIF) campaign, J. Geophys. Res., 112, D24302, doi:10.1029/2007JD008871, 2007.

Prinn, R. G.: Measurement equation for trace chemicals in fluids and solution of its inverse, in Inverse Methods in Global Biogeochemical Cycles, vol. 114, edited by: Kasibhatla, P., Heimann, M., Rayner, P., Mahowald, N., Prinn, R. G., and Hartley, D. E., 3–18, AGU, Washington, D.C., 2000.

Quélo, D., Mallet, V., and Sportisse, B.: Inverse modeling of NO$_x$ emissions at regional scale over northern France: preliminary investigation of the second-order sensitivity. J. Geophys. Res., 110, D24310, doi:10.1029/2005JD006151, 2005.

Rodgers, C. D.: Inverse methods for atmospheric sounding theory and practice, 1st ed., World Scientific, Singapore, 2000.

Russell, A. R., Perring, A. E., Valin, L. C., Hudman, R. C., Browne, E. C., Min, K-E., Wooldridge, P. J., and Cohen, R. C.: A high spatial resolution retrieval of NO$_2$ column densities from OMI: method and evaluation, Atmos. Chem. Phys., 11, 8543–8554, doi:10.5194/acp-11-8543-2011, 2011.

Seinfeld, J. H. and Pandis, S. N.: Atmospheric chemistry and physics, John Wiley & Sons, INC, New Jersey, 209–223, 2006.

Singh, H. B., Brune, W. H., Crawford, J. H., Jacob, D. J., and Russell, P. B.: Overview of the summer 2004 intercontinental chemical transport experiment – North America (INTEX-A). J. Geophys. Res., 111, D24S01, doi:10.1029/2006JD007905, 2006.

TCEQ: Houston-Galveston-Brazoria Attainment Demonstration SIP Revision for the 1997 Eight-Hour Ozone Standard, Austin, TX, chapter 3, 1–35, 2010.

TCEQ.: Dallas-Fort Worth Attainment Demonstration SIP Revision for the 1997 Eight-hour Ozone Standard Non-attainment Area, Austin, TX, chapter 3, 1–31, 2011.

US EPA.: Technical assistance document for the chemiluminescence measurement of nitrogen dioxide, Tech. Rep., Environmental Monitoring and Support Laboratory, US EPA, Research Triangle Park, NC, EPA-600/4-75-003, 1975.

US EPA.: CFR Title 40: Protection of Environment, Part 58-Ambient Air Quality Surveillance, Washington, DC, 2006.

Welch, G. and Bishop, G.: An introduction to the Kalman Filter, University of North Carolina at Chapel Hill, NC, 4–6, 2001.

Xiao, X., Cohan, D. S., Byun, D. W., and Ngan, F.: Highly nonlinear ozone formation in the Houston region and implications for emission controls. J. Geophys. Res., 115, D23309, doi:10.1029/2010JD014435, 2010.

Yarwood, G., Wilson, G., Emery C., and Guenther, A.: Development of the GloBEIS—a state of the science biogenic emissions modeling system. Final Report to the Texas Natural Resource Conservation Commission, Austin, TX, 1999.

Yienger, J. J. and Levy, H.: Empirical-model of global soil-biogenic NO$_x$ emissions. J. Geophys. Res., 100, 11447–11464. doi: 10.1029/95JD00370, 1995.

Zhao, C. and Wang, Y.: Assimilated inversion of NO$_x$ emissions over east Asia using OMI NO$_2$ column measurements. Geophys. Res. Lett., 36, L06805, doi:10.1029/2008GL037123, 2009.